Received: 13 May 2024 | Revised: 24 October 2024 | Accepted: 25 October 2024

DOI: 10.1002/pamm.202400061

RESEARCH ARTICLE

Test rig for validating the integrated motion measurement of flexible beams

Michael Kohl | **Benedikt Györfi** | **Jörg F. Wagner**

Chair of Flight Measuring Technology, University of Stuttgart, Stuttgart, Germany

Correspondence
Michael Kohl, Chair of Flight Measuring Technology, University of Stuttgart, Pfaffenwaldring 31, 70569 Stuttgart.
Email: michael.kohl@pas.uni-stuttgart.de

Abstract

The fundamental principle of integrated motion measurement (IMM) is integrated navigation with inertial sensors combined with, for example, a satellite navigation receiver. Accordingly, IMM makes use of the specific advantages of complementary sensors and blends them in a filter algorithm. To meet requirements in advanced motion measurements, for instance, for structural health monitoring or for structural control purposes, the approach of a single rigid body like in classical navigation no longer holds for IMM. As a solution, additional degrees of freedom (DOFs) for the moving structure are introduced, which represent deformations and allow the navigated body to be treated as a flexible structure. To cover a variety of flexible deformation shapes, a sufficient number of distributed inertial sensors is required. To restrict accumulating errors of these sensors, additional structural measurements for aiding are necessary. The signals of the inertial sensors and the aiding measurements are fused by an extended Kalman filter (EKF) to obtain an optimal estimation of the usual navigation states, extended by the deformation variables. The contribution presents the preparation of the experimental validation of an IMM system for a flexible structure, which represents an idealization of a wing or rotor blade by a movable beam. The mechanical and electrical setup of a test rig is described. Furthermore, the simulation of the test configuration, that is the model of a test beam with a variety of distributed sensors for generating artificial measurements as a test reference, is discussed. Finally, for an optimal sensor placement, the two methods of effective independence and maximization of modal energy are compared and experimentally tested for different amounts of additional flexible DOFs.

1 | INTRODUCTION

With rising development of micro electronic mechanical systems (MEMS) and inertial measurement units (IMUs) and with the constant improvement of GNSS (global navigation satellite system) accuracy and measurements, the usage of inertial navigation systems (INS) – especially in combination with aiding by GNSS – has increased strongly in the past

decades. Wide-ranging applications in cars, robotics, ships, air- and space-craft (e.g., interplanetary missions), and in the military (e.g., missile guidance) as well as short and long-term accuracy are still important topics in navigation application and are under constant research [1, 2].

In this context, the extension of aided inertial navigation with the inclusion of structural deformation and distributed sensors is highlighted here. Wagner [3] worked on a general framework for distributed sensors and flexible structures, with preceding publications dealing with improving the accuracy by arranging several IMUs over the structure of the navigated body [4] or by improving the system architecture [5]. Building on this, Örtel proposed an integrated motion measurement system (IMMS) for flexible structures [6] with sensor placement approaches, simulative proof, and a small scale experimental validation of a clamped cantilever beam [7]. This included the expansion of kinematical models of the structure and a comparison of peripheral sensor types [8]. Kaswekar [9] continued this work to extend the theory to complex lightweight structures with wider research into, for example, sensor placement. Despite the conducted experimental validation on a clamped cantilever beam, a large scale experiment still remains open.

This paper describes the theoretical and experimental setup to provide this large scale experimental validation of integrated motion measurement (IMM) of flexible structures based on the example of a flexible, movable beam pendulum. Section 2 presents a short introduction into the basics of IMM with the relevant sensor signals, system models, and architecture as well as the extension to flexible deformations. The theoretical and experimental design including the underlying model and the resulting conception of the test rig and measurement system is discussed in Section 3. A short discussion of the simulation model and two different approaches to sensor placement complete that section. First measurement results are illustrated and discussed in Section 4. The paper is completed with a short conclusion and an outlook on future research projects in Section 5.

2 | BASICS OF IMM

The approach of IMM originates from classical integrated navigation systems, where the navigated body is treated as a rigid body. Its location is thus described by a maximum of six degrees of freedom (DOFs), namely three DOFs for the spatial position $\mathbf{r}$ and three DOFs for the attitude $\boldsymbol{\Theta}$. The navigation task usually consists of tracking the state vector $\mathbf{x}$ with

$$\mathbf{x} = \begin{bmatrix} \mathbf{r} \\ \dot{\mathbf{r}} \\ \boldsymbol{\Theta} \\ \vdots \end{bmatrix}, \tag{1}$$

which is expanded by the velocity of the object $\dot{\mathbf{r}}$. The state vector usually contains additional parameters like sensor biases, which are left out for a better overview. The propagation and observation of $\mathbf{x}$ is modeled by the equations

$$\begin{aligned} \dot{\mathbf{x}} &= \mathbf{f}(\mathbf{x}, \mathbf{u}) + \mathbf{G}\,\mathbf{w} \quad \text{and} \\ \mathbf{y} &= \mathbf{h}(\mathbf{x}, \mathbf{u}) + \mathbf{v} \end{aligned} \tag{2}$$

with the input vector $\mathbf{u}$ and the aiding vector $\mathbf{y}$. The measurement noise of input and aiding is modeled with the stochastic variables $\mathbf{w}$ and $\mathbf{v}$ respectively. The noise matrix $\mathbf{G}$ maps the input noise to the propagation of the state vector. Typically, IMUs deliver the system input $\mathbf{u}$ by measuring the inertial values accelerations and angular rates. From these measurements, the system state $\mathbf{x}$ can be calculated from Equation (2) by integration and transformation into the desired coordinate systems. Since the numerical solution of these differential equations in combination with usually noisy measurements leads to errors, aiding by complementary measurements becomes necessary. GNSS-measurements are prominent members of such aiding, observing measurements being represented by $\mathbf{y}$ in Equation (2) [2, 5].

2.1 | System architecture and sensor fusion

Generally speaking, the fundamental idea in IMM, or integrated navigation, is to combine different sensor types, where the advantages of one type of sensor are used to compensate for the disadvantages of the other sensor type [2]. In the

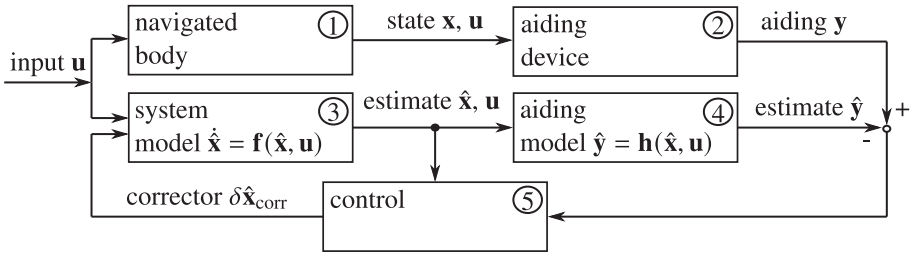

FIGURE 1 System architecture for integrated navigation and IMM systems. Adapted from Wagner [5]. IMM: integrated motion measurement.

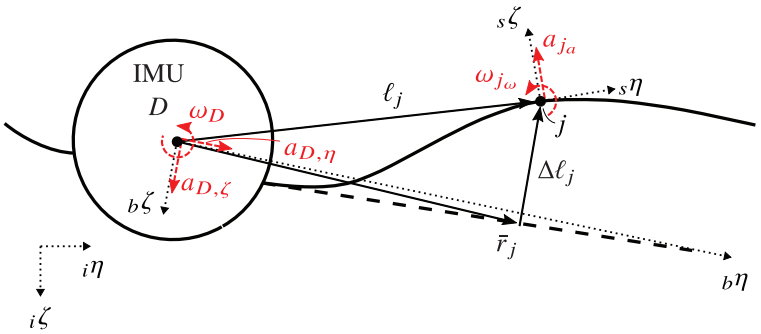

FIGURE 2 Deformed structure with additional peripheral sensors, relevant measurements (red, dashed arrows) and relevant coordinate systems (dotted arrows): inertial system $({}_i\eta, {}_i\zeta)$, body system $({}_b\eta, {}_b\zeta)$ and sensor system $({}_s\eta, {}_s\zeta)$. Adapted from Örtel [6].

case of inertial navigation, the high frequency but error prone output of the IMU is combined with the low frequency but long-term precise output of the GNSS measurements. For solving the differential equations in (2) and sensor fusion of $\mathbf{u}$ and $\mathbf{y}$, an extended Kalman filter (EKF) can be used. In the implementation at hand, the system architecture depicted in Figure 1 [5] is used.

In this case, the navigated body in block ① is subjugated to the measured accelerations and angular rates from the input $\mathbf{u}$, which results in the aforementioned system state $\mathbf{x}$. Simultaneously, the IMMS calculates an estimate of the system state $\hat{\mathbf{x}}$ based on the system model in (2) in block ③. Based on the current system state, the aiding device delivers aiding measurements $\mathbf{y}$ in block ②, for which also an equivalent estimate $\hat{\mathbf{y}}$ is calculated based on Equation (2) in block ④. The difference $\mathbf{y} - \hat{\mathbf{y}}$ is then used to correct the state estimate $\hat{\mathbf{x}}$ via a feedback unit in block ⑤ [5].

2.2 | Additional DOFs in integrated motion measurement

It has been demonstrated that the accuracy of such IMMS or INS can be improved by distributing additional sensors over the navigated structure. However, with distributed sensors, it is questionable whether the rigid body assumption is still reasonable. Especially with increasing size of the structure, the lever arm of additional sensors becomes more and more flexible, which needs to be taken into account in the system model [4].

Figure 2 sketches the cross-section of half an airplane as an example for a structure with an IMMS. One wing is depicted in its undeformed (dashed line) and deformed state (solid line). The fuselage is equipped with an IMU in its center D and additional peripheral sensors j are placed on arbitrary positions on the wing with distance $\boldsymbol{\ell}_j$ from the center D. The distance can be split into a rigid part of the undeformed wing $\bar{\mathbf{r}}_j$ and an elastic, time-dependent part $\Delta\boldsymbol{\ell}_j(t)$. Furthermore, the inertial coordinate system $({}_i\eta, {}_i\zeta)$ as well as the body $({}_b\eta, {}_b\zeta)$ and sensor $({}_s\eta, {}_s\zeta)$ coordinate systems are plotted with dotted arrows. The IMU in D measures the accelerations $a_{D,\eta}$ and $a_{D,\zeta}$ (contained in $\ddot{\mathbf{r}}_D$) and angular rate ω_D (contained in $\boldsymbol{\omega}_{bi}$), relevant for the sketched 2D case. If the additional peripheral sensor is an accelerometer, j becomes j_a and measures i.a. the acceleration a_{j_a} in $\ddot{\mathbf{r}}_{j_a}$. If the additional peripheral sensor is an angular rate sensor (gyroscope), j becomes j_ω and measures the angular rate ω_{j_ω} in $\boldsymbol{\omega}_{j_\omega,si}$. Thus, the depicted measurement variables in Figure 2 are all measured by inertial sensors, meaning that these variables are physical quantities with respect to the inertial coordinate system i, measured in

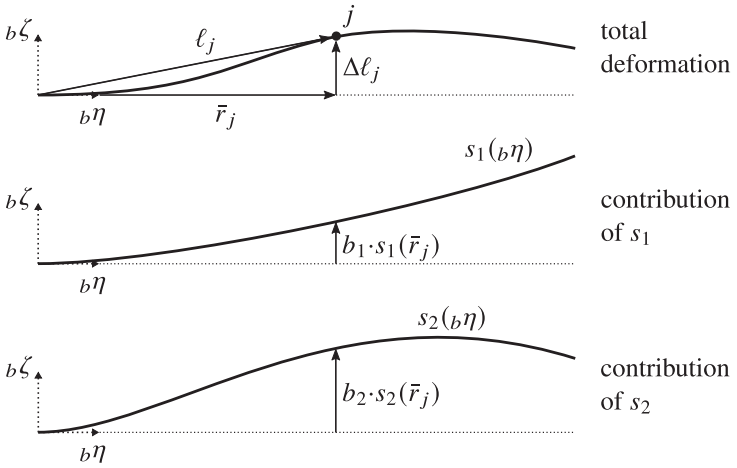

FIGURE 3 Resulting deformation of structure (top) superposed from exemplary first (middle) and second (bottom) unit deformation and deformation variable b_χ in simplified body coordinate system $(_b\eta, _b\zeta)$ with exemplary position of peripheral sensor j. Adapted from Örtel [6].

the according coordinate system of the sensor (b or s). Depending on its type, each peripheral sensor is subjugated to an acceleration or angular rate:

$$\begin{aligned} &\text{accelerometer:} && {}^i\ddot{\mathbf{r}}_{j_a} = {}^i\ddot{\mathbf{r}}_D + {}^b\ddot{\boldsymbol{\ell}}_D + 2\left(\boldsymbol{\omega}_{bi} \times {}^b\dot{\boldsymbol{\ell}}_{j_a}\right) + {}^i\dot{\boldsymbol{\omega}}_{bi} \times \boldsymbol{\ell}_{j_a} + \boldsymbol{\omega}_{bi} \times \left(\boldsymbol{\omega}_{bi} \times \boldsymbol{\ell}_{j_a}\right) \\ &\text{gyroscope:} && \boldsymbol{\omega}_{j_\omega,si} = \boldsymbol{\omega}_{bi} + \frac{1}{2}\frac{\mathrm{d}\left(\mathrm{rot}\,\boldsymbol{\ell}_{j_\omega}\right)}{\mathrm{d}t}. \end{aligned} \tag{3}$$

The left superscripts in Equation (3) refer to the coordinate system, in which differentiation takes place. The unknown lever arm $\boldsymbol{\ell}_j$ is modeled with a series approach

$$\boldsymbol{\ell}_j = \bar{\mathbf{r}}_j + \Delta\boldsymbol{\ell}_j(t) \approx \bar{\mathbf{r}}_j + \sum_{\chi=1}^{\Gamma}\left(b_\chi(t) \cdot \mathbf{s}_\chi\left(\bar{\mathbf{r}}_j\right)\right), \tag{4}$$

where the elastic part $\Delta\boldsymbol{\ell}_j$ is thus the sum of so called unit deformations $\mathbf{s}_\chi\left(\bar{\mathbf{r}}_j\right)$ times their associated, time-dependent deformation variables $b_\chi(t)$. The flexure of the wing at any time can then be represented by a superposition of each involved unit deformation ($\chi = 1, \ldots, \Gamma$) times the current value b_χ of the associated deformation variable as indicated in Figure 3, with Γ being thus the number of considered unit-deformations. A useful but not mandatory choice for unit-deformations are the modeshapes of the structure [6–8].

By substituting Equation (4) and its derivatives $\dot{\boldsymbol{\ell}}_j$ and $\ddot{\boldsymbol{\ell}}_j$ into (3), a relation for the second and first derivative of all $b_\chi(t)$ can be derived with

$$\begin{aligned} &\text{accelerometer:} && \ddot{b}_\chi(t) = f\left(\ddot{\mathbf{r}}_j, \ddot{\mathbf{r}}_D, \boldsymbol{\omega}_{bi}, \ldots, \dot{b}_\chi, b_\chi, \mathbf{s}_\chi\right) \\ &\text{gyroscope:} && \dot{b}_\chi(t) = f\left(\boldsymbol{\omega}_{bi}, \boldsymbol{\omega}_{j_\omega,si}, \ldots, \mathrm{rot}\,\mathbf{s}_\chi\right). \end{aligned} \tag{5}$$

Ultimately, the state vector of Equation (1) can be expanded by the vectors $\mathbf{b}$ and $\dot{\mathbf{b}}$ for accelerometers or $\mathbf{b}$ for gyroscopes to match the general form of Equation (2) with $\mathbf{b}$ and $\dot{\mathbf{b}}$ containing the considered deformation variables and their derivatives. The measurements of the additional peripheral accelerometers or gyroscopes expand the input vector $\mathbf{u}$. In general the number of peripheral sensors must be equal or bigger than the number of considered unit deformations Γ to solve the resulting system of equations [6–8].

3 | THEORETICAL AND EXPERIMENTAL APPROACH

For an experimental validation of the theory above, the aircraft fuselage and wing structure from Figure 2 is simplified to a movable pendulum as depicted in Figure 4. The pendulum bearing represents the center of the aircraft fuselage D

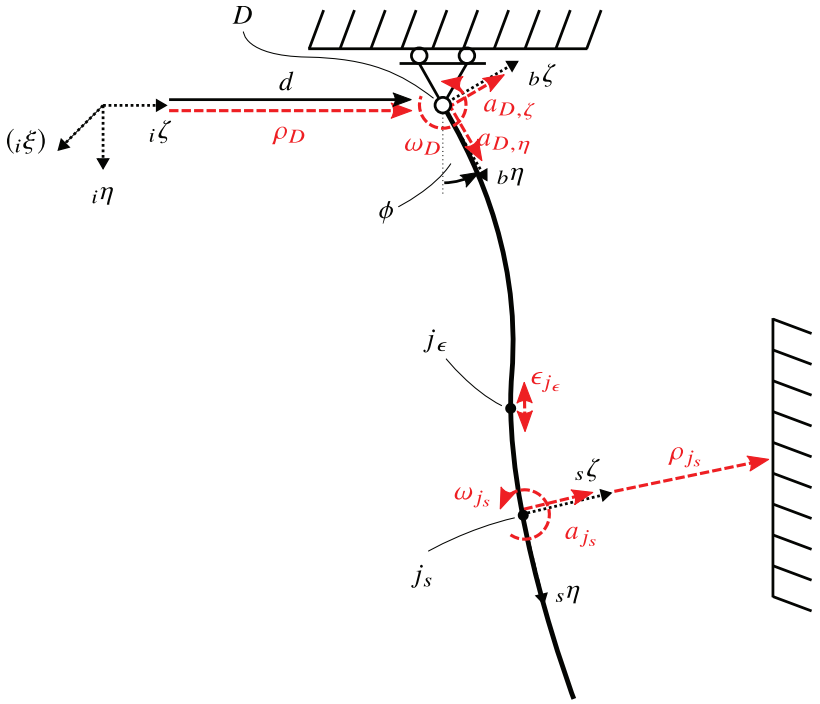

FIGURE 4 Theoretical setup for the experimental IMMS with measurements (red, dashed arrows), relevant coordinate systems (dotted arrows) and selected state variables (d and ϕ). IMMS: integrated motion measurement system.

and the pendulum itself represents one wing of the aircraft. As described in Section 2.2, an IMU is placed in the bearing, measuring the relevant accelerations $a_{D,\eta}$, $a_{D,\zeta}$ as well as the angular rate ω_D. Additional peripheral accelerometers and gyroscopes are implemented by placing IMUs j_s, measuring the depicted relevant acceleration a_{j_s} and angular rate ω_{j_s}. Since the additional peripheral accelerometers and gyroscopes from Section 2.2 are bundled into one sensor unit (the IMU), the indices j_a and j_ω are unified to j_s. Since the pendulum is realized by an indoor test rig with restricted GNSS visibility, distance sensors are used for aiding measurements. A high precision distance sensor measures the displacement ρ_D of the bearing to ensure good comparability between different measurements and simulations. It serves as reference transducer. Time-of-Flight (ToF) distance sensors are placed alongside the peripheral IMUs to measure the distance ρ_{j_s} between the moving sensors and a reference plane. They provide the primary aiding. For additional structurally integrated aiding, strain gauges j_ϵ measure the bending strain ϵ_{j_ϵ}. Strain gauges and peripheral IMUs can not be placed on the same position (see Section 3.2).

Figure 4 also illustrates two of the navigation state variables d and ϕ, which are remnants of the classic navigational DOFs spatial position ($_i\mathbf{r}_D$) and attitude ($\boldsymbol{\Theta}_D$) [7, 8].

This setup enables the evaluation of different IMMS configurations with peripheral accelerometers (acc) or alternatively peripheral gyroscopes (gyro), which complete the state, input, and aiding vectors from Equations (1) and (2) with

$$\mathbf{x}_{acc} = \begin{bmatrix} {}_i\mathbf{r}_D \\ {}_i\dot{\mathbf{r}}_D \\ \boldsymbol{\Theta}_D \\ \mathbf{b} \\ \dot{\mathbf{b}} \\ \vdots \end{bmatrix}, \mathbf{x}_{gyro} = \begin{bmatrix} {}_i\mathbf{r}_D \\ {}_i\dot{\mathbf{r}}_D \\ \boldsymbol{\Theta}_D \\ \mathbf{b} \\ \vdots \end{bmatrix}, \mathbf{u}_{acc} = \begin{bmatrix} a_{D,\eta} \\ a_{D,\zeta} \\ \omega_D \\ \dot{\omega}_D \\ \mathbf{a} \end{bmatrix}, \mathbf{u}_{gyro} = \begin{bmatrix} a_{D,\eta} \\ a_{D,\zeta} \\ \omega_D \\ \boldsymbol{\omega} \end{bmatrix}, \mathbf{y}_{acc} = \mathbf{y}_{gyro} = \begin{bmatrix} \rho_D \\ \dot{\rho}_D \\ \boldsymbol{\rho} \\ \boldsymbol{\epsilon} \end{bmatrix} \tag{6}$$

with the vectors $\mathbf{a}$, $\boldsymbol{\omega}$, $\boldsymbol{\rho}$ and $\boldsymbol{\epsilon}$ containing all additional peripheral accelerometer, gyroscope, distance sensor, and strain gauge measurements respectively. The derivatives $\dot{\omega}_D$ and $\dot{\rho}_D$ are not measured directly but can be obtained from a difference quotient of the respective measurements [6–8].

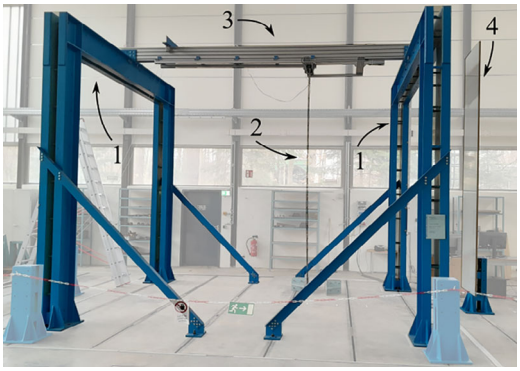

FIGURE 5 Steel frame (1) with movable pendulum (2) on aluminum beam (3) and reflective surface wall (4).

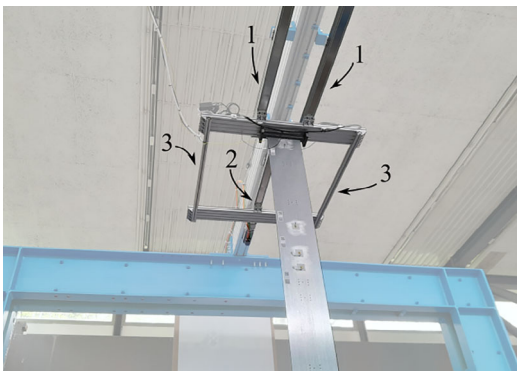

FIGURE 6 Pendulum suspension with two linear guidance rails (1), connected to linear actuator (2) via two transmission bars (3).

3.1 | Test rig setup

For practical implementation, a construction for supporting such a pendulum, which is large, movable, and ideally controllable at the bearing along one axis, is needed. The authors have chosen a steel frame construction consisting of two opposing portals and a reflective surface wall for the ToF distance sensors as shown in Figure 5. The two portals are connected by an aluminum beam on top, which holds the pendulum suspension. The pendulum is a steel sheet of the material DX51D+Z with dimensions 4 m × 20 cm × 0.2 cm.

The pendulum suspension itself, shown in Figure 6, consists of two linear guidance rails mounted on the bottom of the aluminum beam. The rails are used to allow displacements along one axis and suppress as much transverse movements of the pendulum as possible in order to keep its motion in the ${}_i\eta,{}_i\zeta$-plane as depicted in Figure 4. The guidance rails carry the bearing/base D of the pendulum on a vertical mounting device, which is connected by two bars to a linear actuator mounted in series to the guidance rails. The bars transmit the movement of the actuator to the pendulum to realize pendulum displacements. The pendulum rotation ϕ is realized by a plain bearing.

The linear actuator is the make ITEM KGT 6 60 P20-600 and can impose defined movements $d(t)$ (see Figure 4) on the pendulum bearing D to ensure comparability between different measurements and simulations for validation. The actuator gives the possibility to target desired way points with distinct accelerations, decelerations, and maximum velocity. By analyzing turning points and extremal points of a desired distance function $d(t)$, an approximation of that function can be recreated and repeatedly activated as illustrated in Figure 7. In this way, different frequencies or excitations, such as the eigenfrequencies of the beam, can be superposed as well as any arbitrary excitation can be approximated.

3.2 | Measurement system

To obtain the measurements of accelerations, angular rates, distances, and bending strains according to Equation (6), at multiple positions and at synchronous time steps, a sophisticated measurement system is necessary. For that, a solution

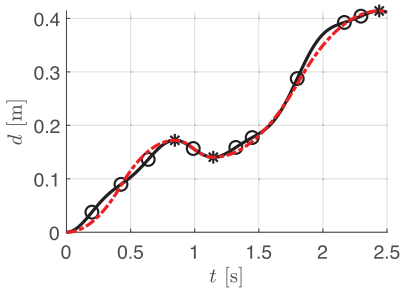

FIGURE 7 Exemplary actuator target function (solid line) with extremal values (*), turning points (o) and approximation realized by the actuator (red, dash-dotted line).

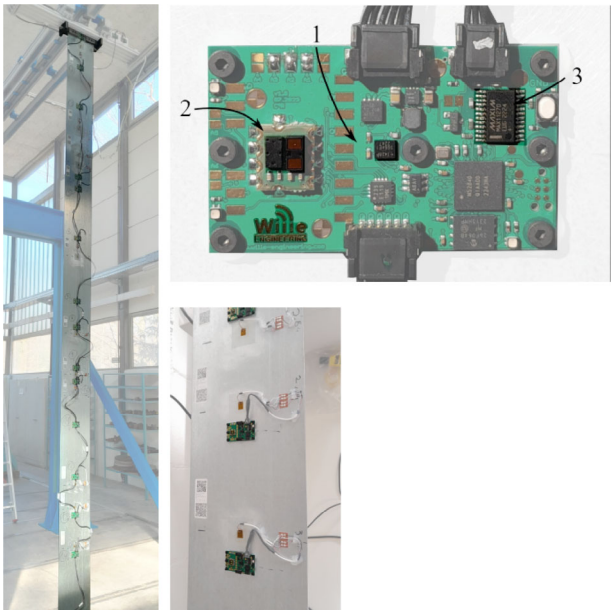

FIGURE 8 Left: Pendulum equipped with full configuration of interconnected PCBs. Top right: Single PCB with IMU (1), ToF distance sensors (2) and ADC (3). Bottom right: Unconnected PCBs with strain gauges. ADC: analogue to digital converter; IMU: inertial measurement unit; PCB: printed circuit boards.

with multiple interconnected printed circuit boards (PCBs) was developed by the company WILLE ENGINEERING, (Hattersheim am Main, Germany), with an exemplary arrangement on the pendulum shown on the left picture in Figure 8. Each PCB houses a TDK InvenSense ICM-42688-P MEMS IMU [10], two independent ToF distance sensors VL53L1X [11], and VL53L4CX [12] by STMicroelectronics as well as an Analog Devices MAX11270 [13] analogue to digital converter (ADC) as interface to strain gauges. In order to measure bending strains isolated from tensile strains of the beam, the strain gauges at every measuring location form a wheatstone full bridge. A single PCB is shown on the top right in Figure 8 and three PCBs with visible strain gauges in their vicinity are displayed on the bottom right picture. The measurement system is completed by the high precision linear distance sensor LMFA/LMKA 3010 by AMO Automatisierung Messtechnik Optik GmbH, mounted between the pendulum suspension and the aluminum beam of the test rig.

The measurement system gives thus the possibility to measure all desired parameters described in Section 3. The PCBs can be mounted and connected with variable number and position and can be used to create different configurations of combinations of sensor type and position. Each PCB has a connector to its preceding PCB on top and to its subsequent PCB on the bottom of the board while creating a daisy chain of interconnected PCBs. At the top of the chain there is an additional master PCB followed by another extra PCB that reads measurements from the high precision linear distance sensor. To ensure synchronous measurements, the master PCB sends trigger signals to the other PCBs (timed to the desired sample rate of the IMMS). With each trigger signal, each PCB stores the current measurement data. At the end of each test trial, the stored data can be read out with unified timestamps.

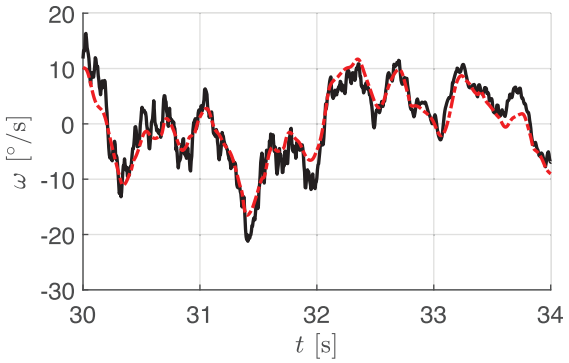

FIGURE 9 Comparison of one gyroscope measurement output (solid line) with its equivalent simulated artificial measurement (red, dash-dotted line).

3.3 | Simulation model

To validate the results of the described IMMS, a comparative simulation is necessary. For that, a discretized Finite Element (FE) model of the system depicted in Figure 4 was created in ANSYS. The model consists predominantly of Timoshenko beam elements to model the beam-like structure of the pendulum. Three different types of damping were identified as dominant during initial trials and measurements. First, the friction in the rotational DOF of the bearing was modeled with Coulomb friction. Second, the most dominant part of the damping results from the air resistance against the relatively large flow area of the pendulum was modeled by viscous dashpot damping proportional to the velocity squared. Third, the internal material damping of the structure was modeled with Rayleigh-Damping. To ensure good comparability between the FE simulation and measurement data, an optimization of the simulation model in ANSYS had to be done. The optimization tuned the friction parameters as well as the thickness of the pendulum to account for the influence of the measurement system. The optimization was based on minimizing the root mean square error between artificial measurements from the FE simulation and real measurements directly obtained from the measurement system. Figure 9 compares the real measurement of an arbitrarily picked gyroscope and its simulated artificial counterpart calculated with simulation parameters obtained from the optimization.

3.4 | Sensor placement

For sensor placement two different approaches as already investigated by Örtel [6] and Kaswekar [9] are used for creating pendulum configurations as the one shown on the left side of Figure 8. Both methods use a modal representation of the linearized system of Equation (2) around its stable equilibrium state. For accelerometers and distance sensors, the displacements of the mode shapes are used. Gyroscopes use the twists and strain gauges the bending of the mode shapes. Both methods start with a set of potential sensor locations where unsuitable sensor positions are sequentially deleted.

First, maximization of modal energy is the criteria for placing sensors. It is based on maximizing modal norms of the modal state-space representation of the linearized system of Equation (2). By, for example, maximizing the observability of the system (by maximizing the Hankel norm), potential sensor locations with low norms are deleted until the desired number of sensors is reached [9, 14].

Second, the Effective Independence (EI) successively removes potential sensor locations that contribute least to the linear independence of the targeted mode shapes [6, 9, 15].

Depending on the selected number of additional peripheral sensors and on the selected method of sensor placement, an individual measurement configuration is created. To evaluate different placement methods, sensor types, and the number of additional DOFs, each configuration was realized with the PCBs to evaluate as many different scenarios as possible.

4 | RESULTS

For the first system tests and evaluation results, a displacement function $d(t)$ with frequency components in the vicinity of the first three eigenfrequencies of the beam was assigned to the linear actuator described in Section 3.1. After an initial rest

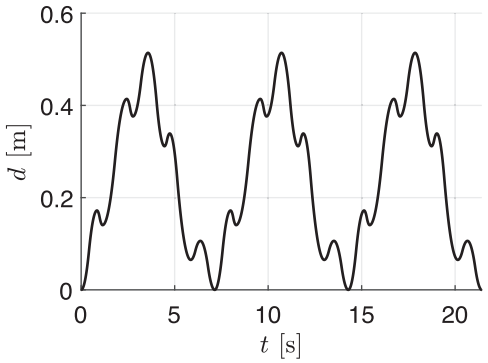

FIGURE 10 Section of the distance function of one sequence of excitation via the linear actuator.

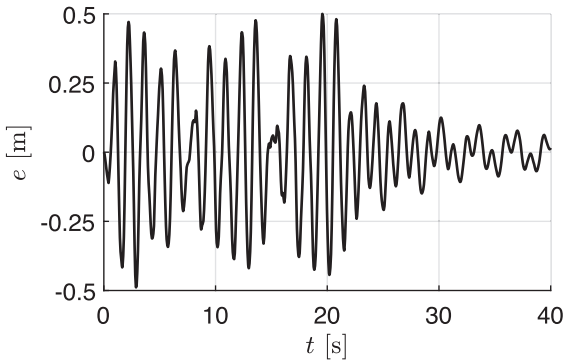

FIGURE 11 Pseudo-elastic deformation e at the lower end of the pendulum for a gyroscope IMMS with four peripheral sensors. IMMS: integrated motion measurement system.

phase of 60 s for the IMMS to get settled, this displacement function consists of three equal sequences with one sequence shown in Figure 10. The first two eigenfrequencies have the most significant contribution to the displacement function. Each sequence is followed by a rest phase of the actuator of 20 s. In total, four different test trials with this setup were investigated. The measurement system was configured in a way that optimal accelerometer and gyroscope placement for three and four peripheral sensors was determined according to the criteria of the EI method.

For evaluating the estimation error of the introduced deformation variables, the pseudo-elastic deformation e at the lower end of the pendulum is evaluated. The pseudo-elastic deformation is an indication for the deflection of the pendulum excluding the attitude ϕ and the displacement d of the base, thus offering insight into the estimation quality of the additional DOFs $\mathbf{b}$. In the case, presented in this paper, e equals $\Delta\ell(t)$ from Equation (4). The results of e for a setup with four peripheral gyroscopes only are plotted in Figure 11 for the first sequence of excitation and rest phase. The initial 60 s are not considered here. The associated pseudo-elastic deformation error Δe between IMMS and simulation for the entire test period is plotted in Figure 12.

Finally, the standard deviations $\sigma_{\Delta e}$ of the pseudo-elastic deformation errors over the test periods are shown. Figure 13 compares means of $\sigma_{\Delta e}$ over all four test trials for different numbers of peripheral sensors and types of peripheral sensors used. The accelerometer and gyroscope placements of the configurations with one and two sensors were chosen according to the criteria of the EI method from the available sensors of the previously created pendulum configuration.

Figure 13 indicates that gyroscopes as peripheral sensors are superior to accelerometers. Since accelerometers need a double instead of a single integration (see Equation (5)), a higher numerical error of accelerometers is to be expected. Reaching a limit in accuracy after two or three peripheral sensors can be explained with the excitation including only the first three eigenfrequencies. Higher mode shapes and thus unit-deformations are not excited; therefore, more included unit-deformations are not improving the accuracy any further.

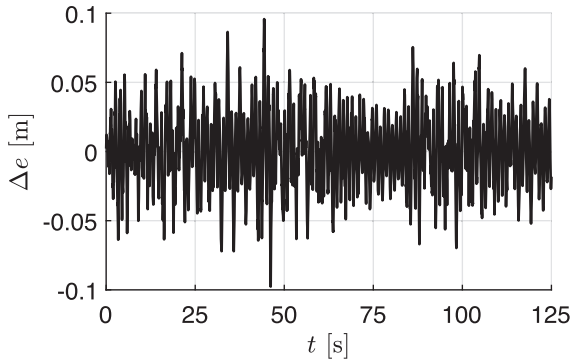

FIGURE 12 Pseudo-elastic deformation error $\sigma_{\Delta e}$ at the lower end of the pendulum for a gyroscope IMMS with four peripheral sensors. IMMS: integrated motion measurement system.

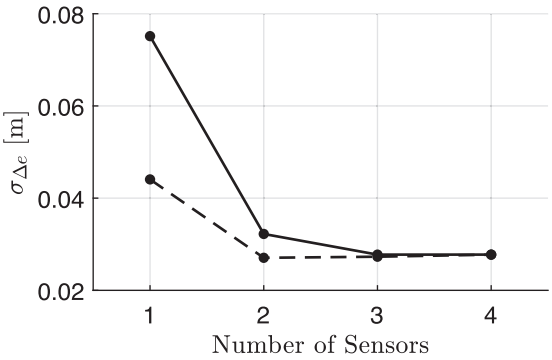

FIGURE 13 Mean standard deviation for EI accelerometer (solid line) and EI gyroscope (dashed line) placement.

5 | CONCLUSION

The test rig with its measurement system gives the possibility to experimentally extend the simulative validation of the IMMS approach for flexible bodies on the example of a flexible, movable beam. The core of the test rig is the sensor array, allowing synchronous measurements at a multitude of sensor locations. With multiple circuit boards housing different sensor types, a variety of pendulum configurations can be created, thus enabling to compare different sensor placement methods and different types of peripheral sensors under variable, controllable excitation. Artificial measurements, obtained from FE simulations, show good agreement to the real measurement data, justifying the evaluation of the obtained deformation variables. In addition, simulative results and first experiments indicate a superiority of gyroscopes over accelerometers in the estimation of structural deformations.

In upcoming research, the validation of IMMS for flexible bodies according to Örtel [6] will be completed. Building on that, further projects will expand the system to advanced tasks such as structural health monitoring and control.

ACKNOWLEDGMENTS

Open access funding enabled and organized by Projekt DEAL.

ORCID

Michael Kohl https://orcid.org/0009-0000-6512-6219
Jörg F. Wagner https://orcid.org/0000-0002-8536-4668

REFERENCES

1. Farrell, J. A., & Barth, M. (2000). *The global positioning system and inertial navigation*. McGraw-Hill.
2. Titterton, D. H., & Weston, J. L. (2004). *Strapdown inertial navigation technology* (2 ed.). Institution of Electrical Engineers and American Institute of Aeronautics and Astronautics.

3. Wagner, J. F. (2003). *Zur Verallgemeinerung integrierter Navigationssysteme auf räumlich verteilte Sensoren und flexible Fahrzeugstrukturen*. VDI-Verlag.
4. Wagner, J. F., & Kasties, G. (2002). Improving the GPS/INS integrated system performance by increasing the distance between GPS antennas and inertial sensors. In *Proceedings of the 2002 national technical meeting of the institute of navigation* (pp. 103–115). ION.
5. Wagner, J. F., & Wieneke, T. (2003). Integrating satellite and inertial navigation – conventional and new fusion approaches. *Control Engineering Practice*, *11*(5), 543–550.
6. Örtel, T. (2010). *Integrierte Bewegungsmessung an flexiblen Strukturen*. Verlag Dr. Hut.
7. Örtel, T., Wagner, J. F., & Saupe, F. (2013). Integrated motion measurement illustrated by a cantilever beam. *Mechanical Systems and Signal Processing*, *34*(1-2), 131–145.
8. Wagner, J. F., & Örtel, T. (2008). Accelerometers versa gyros in integrated navigation systems for flexible vehicles. *In Proceedings of the 2008 national technical meeting of the institute of navigation* (pp. 689–698). ION.
9. Kaswekar, P. (2017). *Integrated motion measurement of three-dimensional lightweight structures*. Verlag Dr. Hut.
10. TDK InvenSense (2010). ICM-42688-P Datasheet: High Precision 6-Axis MEMS MotionTracking™Device, Rev. 1.7.
11. STMicroelectronics (2022). VL53L1X: A new generation, long distance ranging Time-of-Flight sensor based on ST's FlightSense technology, Rev. 7.
12. STMicroelectronics (2022). VL53L4CX: Time-of-Flight sensor with extended range measurement, Rev. 4.
13. Analog Devices (2015). MAX11270: 24-Bit, 10mW, 130dB SNR, 64ksps Delta-Sigma ADC with Integrated PGA, Rev. 1.
14. Gawronski, W. K. (2004). *Advanced structural dynamics and active control of structures*. Springer.
15. Kammer, D. C. (1991). Sensor placement for on-orbit modal identification and correlation of large space structures. *Journal of Guidance, Control, and Dynamics*, *14*(2), 251–259.

How to cite this article: Kohl, M., Györfi, B., & Wagner, J. F. (2024). Test rig for validating the integrated motion measurement of flexible beams. *Proceedings in Applied Mathematics and Mechanics*, *24*, e202400061. https://doi.org/10.1002/pamm.202400061